

Supporting Information

Constructing Multifunctional Virus-Templated Nanoporous Composites for Thin Film Solar Cells: Contributions of Morphology and Optics to Photocurrent Generation

Noémie-Manuelle Dorval Courchesne,^{1,2†} Matthew T. Klug,^{2,3†} Kevin J. Huang,⁴ Mark C. Weidman,¹ Victor J. Cantú,¹ Po-Yen Chen,^{1,2} Steven E. Kooi,⁵ Dong Soo Yun,² William A. Tisdale,¹ Nicholas X. Fang,³ Angela M. Belcher,^{2,4,6} and Paula T. Hammond^{1,2*}*

¹Department of Chemical Engineering, Massachusetts Institute of Technology, Cambridge, MA 02139, United States. ²The David Koch Institute for Integrative Cancer Research, Massachusetts Institute of Technology, Cambridge, MA 02139, United States. ³Department of Mechanical Engineering, Massachusetts Institute of Technology, Cambridge, MA 02139, United States. ⁴Department of Materials Science and Engineering, Massachusetts Institute of Technology, Cambridge, MA 02139, United States. ⁵The Institute for Soldiers Nanotechnologies, Massachusetts Institute of Technology, Cambridge, MA 02139, United States. ⁶Department of Biological Engineering, Massachusetts Institute of Technology, Cambridge, MA 02139, United States.

† These authors contributed equally to this work.

* Corresponding authors: Hammond@mit.edu, 617-258-7577, 77 Massachusetts Avenue, room 76-553, Cambridge, MA, 02139; Belcher@mit.edu, 617-324-3300, 77 Massachusetts Avenue, room 76-561

Film Morphology

Figure S1 presents additional scanning electron microscopy (SEM) images that highlight the interconnected mesh-like morphology of virus-templated titania thin films.

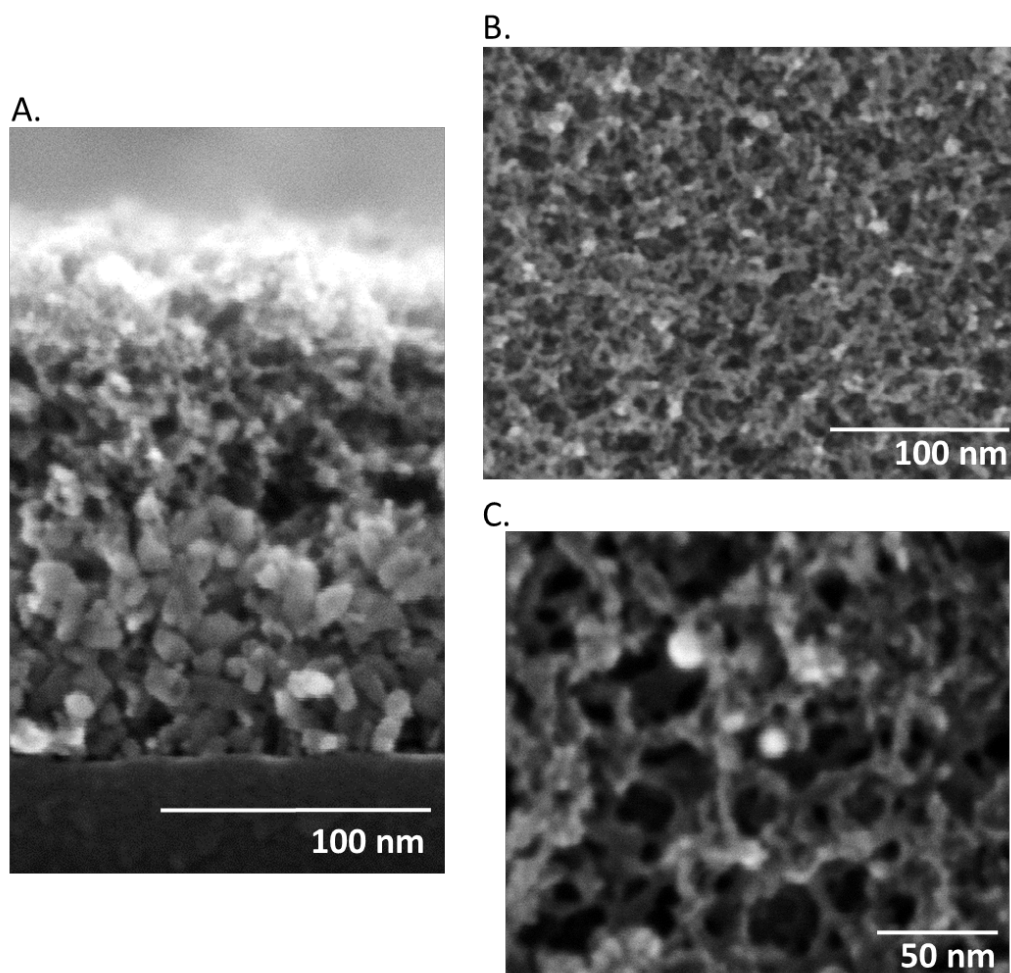


Figure S1. Virus-templated titania films have an interconnected continuous morphology. SEM images showing A. the cross-section of a virus-templated titania film constructed on top of a compact titania paste layer, B. the surface morphology of a virus-templated titania film also containing silver nanoparticles, and C. a high resolution image of the surface morphology of a virus-templated titania film containing gold nanoparticles.

Pore Filling and XPS Depth Profiling

Pore Filling Efficiency Calculation

X-ray photoelectron spectroscopy (XPS) with depth profiling was used to monitor the atomic concentration of lead and titanium as a function of film depth and these atomic concentrations were converted to lead sulfide/titania molar ratios and subsequently to volume fractions using the molecular weight and crystalline density of anatase titania and lead sulfide. First, the mole fractions of lead (Pb) and titanium (Ti) are equal respectively to the mole fractions of lead sulfide (PbS) and titania (TiO₂) and can be taken as the atomic concentrations measured by XPS.

$$n_{PbS} = n_{Pb} \text{ and } n_{TiO_2} = n_{Ti} \quad (S1)$$

$$x_{PbS} = \frac{n_{PbS}}{n_{PbS} + n_{TiO_2}} \times 100\% \quad (S2)$$

$$x_{TiO_2} = \frac{n_{TiO_2}}{n_{PbS} + n_{TiO_2}} \times 100\% \quad (S3)$$

where x_{PbS} and x_{TiO_2} are the mole fractions of lead sulfide and titania respectively, n_{PbS} , n_{Pb} , n_{TiO_2} and n_{Ti} are the number of moles of PbS, Pb, TiO₂ and Ti respectively.

Then, from the known crystalline volumes of anatase titania and lead sulfide, relative volumes of titania and lead sulfide can be calculated on a 100 mol basis.

$$V_{TiO_2} = V_{TiO_2molecule} \times x_{TiO_2} \quad (S4)$$

$$V_{PbS} = V_{PbSmolecule} \times x_{PbS} \quad (S5)$$

where V_{TiO_2} and V_{PbS} are the relative volumes of bulk titania and lead sulfide within the film, and $V_{TiO_2molecule}$ and $V_{PbSmolecule}$ the known volume of a molecule of TiO₂ and PbS in their crystalline phases, respectively.

From this data, the pore filling efficiency, or the percentage of the pores in the titania film that are filled with PbS QDs, was calculated as a function of depth in the titania film. This calculation was done using a measured porosity of 42% for the titania film (see Figure 3B), and assuming that the maximum possible QD packing density inside the pores is a loose random-packing configuration of 56%. A total value for the volume of the blend layer film (including the titania, the loosely-packed PbS and air) can be determined, as well as the volume of the pores within the titania film before infiltration:

$$V_{total} = \frac{V_{TiO_2}}{(1 - \rho_{TiO_2})} \quad (S6)$$

$$V_{pores} = \rho_{TiO_2} \times V_{total} \quad (S7)$$

where V_{TiO_2} is the volume of TiO_2 derived from XPS measurements; ρ_{TiO_2} the known porosity of the titania film; V_{total} the total film volume including TiO_2 , loosely-packed PbS and air; and V_{pores} the volume of the pores within the TiO_2 film before infiltration.

From the packing density of PbS, the volume of loosely-packed quantum dots at each film depth can be calculated, as well as the pore filling fraction, which is simply the ratio of the loosely-packed QD volume over the volume of the pores in the titania film.

$$V_{l-pPbS} = \frac{V_{PbS}}{f_{PbS}} \quad (S8)$$

$$\eta_{filling} = \frac{V_{l-pPbS}}{V_{pores}} \times 100\% \quad (S9)$$

where f_{PbS} is the packing fraction of the quantum dots; V_{PbS} the volume of PbS particles derived from XPS measurements; V_{l-pPbS} the volume of loosely-packed quantum dots; and $\eta_{filling}$ the pore filling efficiency or, in other words, the fraction of the initial volume of the pores in the TiO_2 film that is now filled with PbS QDs taking into account their packing density.

$$V_{PbS} = 52.28 \text{ \AA}^3 \times 82.7 = 905.4 \text{ \AA}^3$$

$$V_{total} = \frac{2817.0 \text{ \AA}^3}{(1 - 0.42)} = 4857.0 \text{ \AA}^3$$

$$V_{pores} = 0.42 \times 4857.0 \text{ \AA}^3 = 2039.9 \text{ \AA}^3$$

$$V_{l-pPbS} = \frac{2817.0 \text{ \AA}^3}{0.56} = 1616.8 \text{ \AA}^3$$

$$\eta_{filling} = \frac{1616.8 \text{ \AA}^3}{2039.9 \text{ \AA}^3} \times 100\% = 79.26\%$$

Low Efficiency Infiltration Methods

A first infiltration study was carried out via dip-coating, with or without ligand exchange (Figure S2A). When the QDs were coated ten times onto a titania film without ligand exchange, very little infiltration occurred, and the QDs did not penetrate further than 30 nm in depth. When an exchange of the oleic acid ligands to benzene-1,3-dithiol (BDT) was performed, the infiltration slightly increased, but a thick PbS QD layer formed on top of the titania film. The adherence of the QDs was thus improved by the exchange with BDT, but the infiltration was marginally affected. A third sample was prepared by dip-coating a titania film that was previously incubated overnight in a 1% mercaptopropionic acid (MPA) solution. This treatment allowed for a deeper infiltration than the control, but since only one dip was done, the pore filling fraction was not improved. Next, an infiltration study was carried out by dropcasting the PbS QDs onto titania films and air-drying the samples (Figure S2B). With and without ligand exchange with MPA, the PbS content within the titania film increased compared to the dip-coat method. With MPA exchanges after each dropcast, the PbS QDs were, again, able to infiltrate deeper into the film. Based on these observations, spincoating and dropcasting methods were compared for a more concentrated PbS QD solution, and with MPA ligand exchange, which yielded the most efficient infiltrations that are presented in Figure 1D. Infiltration methods shown in Figure S1 are less efficient in terms of both PbS content and infiltration depth.

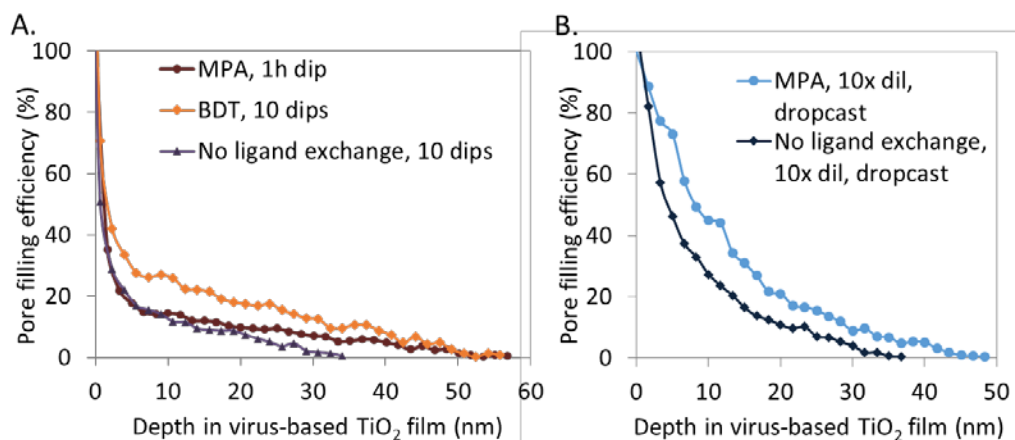


Figure S2. Infiltrating PbS QDs in porous bacteriophage-templated titania films by dip-coating, or dropcasting with a very dilute solution does not result in high PbS content within the titania film. Pore filling efficiencies as a function of film depth calculated from XPS depth profiling results for A. Thin films dip-coated in a 5 mg/mL PbS solution with or without ligand exchange. A sample was first incubated in MPA overnight and then dipped in the PbS QD solution for 1h. The other two samples were dipped successively 10 times in the PbS QD solution with or without exchange with BDT between each dip. B. PbS QDs dropcast onto titania films at 5 mg/mL 10 times with or without exchanging the ligands with MPA between each dropcast.

Thickness Optimization

Device thickness was optimized using planar controls constructed using commercial paste to produce a compact titania layer. The results are shown in Figure S3. These devices differ from the porous titania paste control used for comparison against porous virus-templated devices. Here, the titania layer is compact. No sacrificial polymer was used to create porosity in the structure, and therefore, the resulting device architecture should be approximately planar. No infiltration of PbS QDs within the titania layer is expected here.

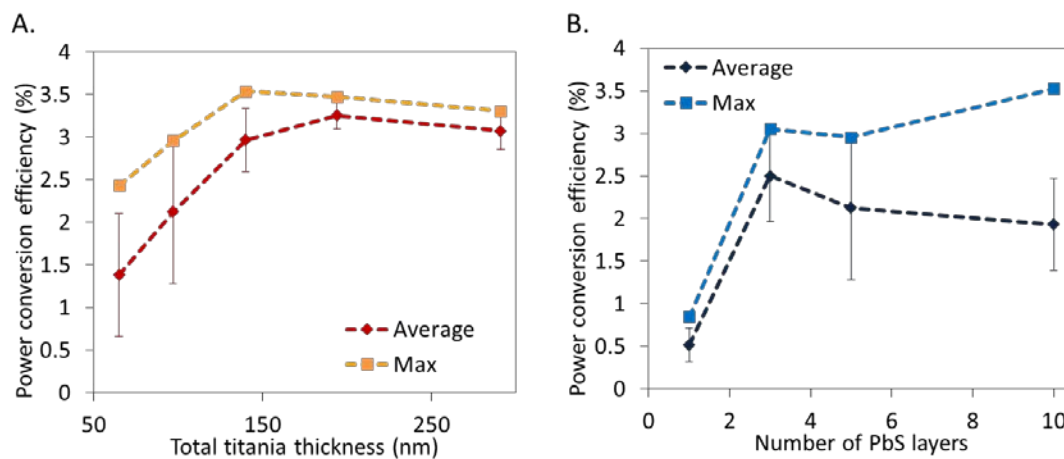


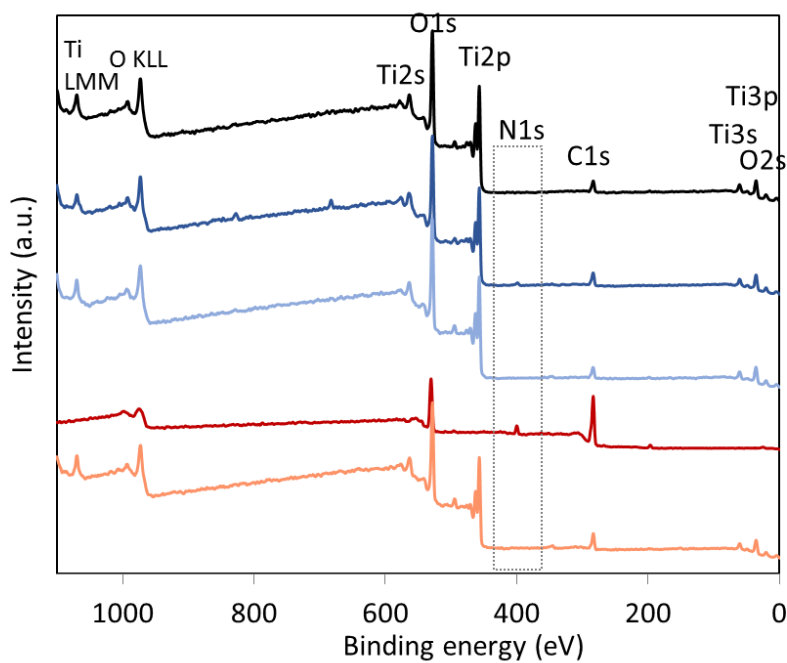
Figure S3. Device performance as a function of the thickness of the titania and PbS layers for a planar device. Maximum and average power conversion efficiency as a function of A. thickness of titania, and B. number of layers of PbS QDs spin-coated.

Surface Functionalization and Series/Shunt Resistances

Polymer Base Layer Removal upon Annealing

Figure S4 and Table S2 respectively show the XPS surveys scans measured before and after annealing, and the resulting atomic composition of the titania surface. When the polymers are deposited, peaks for nitrogen can be observed due to the presence of amine groups in PEI and in PAH. For the samples with PEI, the nitrogen signal is weak and titanium atoms can still be detected, indicating that that PEI layer is, as expected, thinner than 10 nm (maximum detection depth by XPS). For the samples with PAH/PAA base layers, the nitrogen signal is stronger, as well as the carbon signal, but no titania is detected on the surface. This observation confirms that the PAH/PAA base layers are 10 nm thick or greater. Then, after burning off the polymers at 500 °C, the nitrogen peak disappears from all samples, revealing a clear titania surface. It has to be noted that oxygen and carbon are present in all samples (including the titania surface before any polymer is deposited) because of natural oxidation and contamination with carbon.

A.



B.

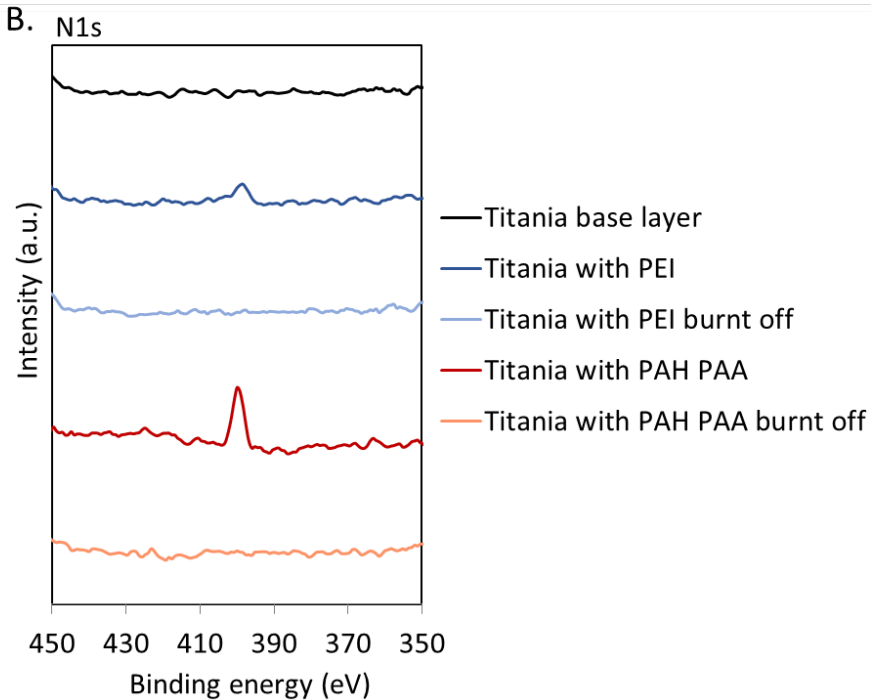


Figure S4. Polymer base layers completely burn off after annealing at 500 °C. XPS surface analysis for a thin PEI layer and PAH/PAA base layers deposited onto compact titania paste. A. Survey scans. B. N1s region of the survey scan showing the disappearance of nitrogen after annealing.

Table S2. Atomic composition of the surface of compact titania or titania with polymer layers gives insights about the presence and thickness of polymer layers. Atomic concentrations of titanium, oxygen, carbon and nitrogen determined by XPS before and after annealing at 500 °C.

Sample	Ti	O	C	N
	(%)	(%)	(%)	(%)
Titania base layer	23.2	59.9	16.8	0
Titania with PEI	21.2	54.0	20.7	4.1
Titania with PEI burnt off	21.8	60.2	18.0	0
Titania with PAH/ PAA	0	31.0	62.5	6.5
Titania with PAH/PAA burnt off	20.1	54.4	25.6	0

Normalized Series and Shunt Resistance Calculation

Series and shunt resistances were calculated from the inverse of the slope of the JV curve at $V = 0$ V and $J = 0$ mA/cm² respectively. The resistances were normalized to the characteristic resistance of the cell, R_{CH} , which is calculated as follows:

$$R_{CH}[\Omega/\text{cm}^2] = \frac{V_{OC}[V]}{J_{SC}[A/\text{cm}^2]} \quad (\text{S10})$$

where V_{OC} is the open circuit voltage and J_{SC} is the short-circuit current density.

Dividing the series and shunt resistances by the cell resistance gives the normalized resistances:

$$r_{SH}[-] = \frac{R_{SH}[\Omega/\text{cm}^2]}{R_{CH}[\Omega/\text{cm}^2]} \quad \text{and} \quad r_{SR}[-] = \frac{R_{SR}[\Omega/\text{cm}^2]}{R_{CH}[\Omega/\text{cm}^2]} \quad (\text{S11})$$

where r_{SH} and r_{SR} are the normalized shunt and series resistances, and R_{SH} and R_{SR} the shunt and series resistances, respectively.

Calculated Resistances for Different Surface Functionalization Methods

Table S3 presents the characteristic resistance, shunt and series resistances for devices constructed using silanes, PAH/PAA base layers of a thin PEI layer as surface functionalization prior to virus film assembly. These values were used to calculate normalized resistances presented in Figures 2C.

Table S3. Calculated characteristic, shunt and series resistances, and normalized resistances for different titania surface functionalization methods.

Surface functionalization	R_{CH} [Ω/cm^2]	R_{SR} [Ω/cm^2]	R_{SH} [Ω/cm^2]	r_{SR}	r_{SH}
Silane	90.1	97.7	95.4	1.08	1.06
PAH/PAA base layers	62.7	42.3	89.6	0.68	1.43
Thin PEI layer	53.8	35.9	88.1	0.67	1.64

Calculated resistances for best optimized devices with or without metal nanoparticles

Table S4 present the resistances calculated for each optimized virus-based devices with or without nanoparticles, and for the paste control device.

Table S4. Calculated characteristic, shunt and series resistances, and normalized resistances for the best optimized devices of each type.

Device	R_{CH} [Ω/cm^2]	R_{SR} [Ω/cm^2]	R_{SH} [Ω/cm^2]	r_{SR}	r_{SH}
Paste control	49.8	27.1	116.9	0.55	2.35
1.5 h, virus only	37.0	26.2	77.2	0.71	2.09
2 h, virus only	34.4	18.0	128.1	0.52	3.73
2.5 h, virus only	37.1	27.0	104.4	0.73	2.82
2 h, with Au NPs	35.7	19.2	163.5	0.54	4.58
2 h, with Ag NPs	33.9	23.9	173.7	0.71	5.12
2 h, with Ag NPLs	33.8	16.5	176.4	0.49	5.21

Estimating Porosity with ImageJ

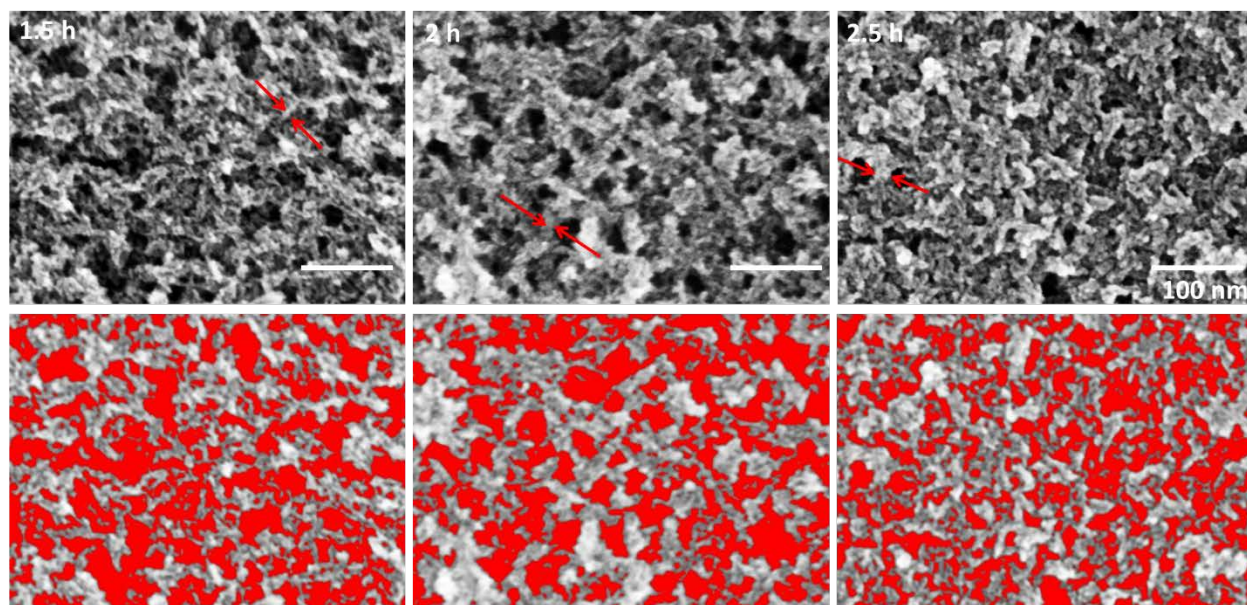


Figure S5. Image analysis for the estimation of porosity, pore size distribution and size of nanowire-like features. The analysis was performed using the ImageJ software. The contrast between the pores and the titania was enhanced (top row), and the area corresponding to the pores was calculated (area in red in the bottom row). To calculate the equivalent diameter of a pore, the area was converted into diameter assuming a circular pore. The red arrows show nanowire features in each image. To determine the average nanowire size, several nanowires were measured in each enhanced-contrast image and the measurements were averaged.

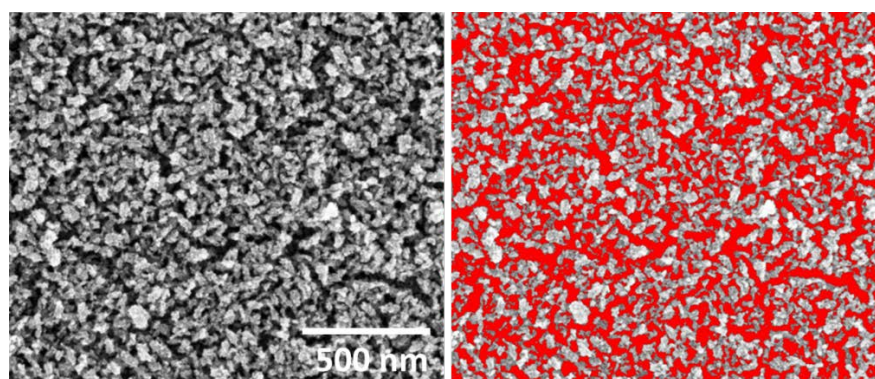


Figure S6. Image analysis of the TiCl_4 -derived TiO_2 paste film. The analysis was performed with the ImageJ software to estimate the film porosity as described in Figure S1.

Silver Nanoplates: Morphology and Effects on Device Performance

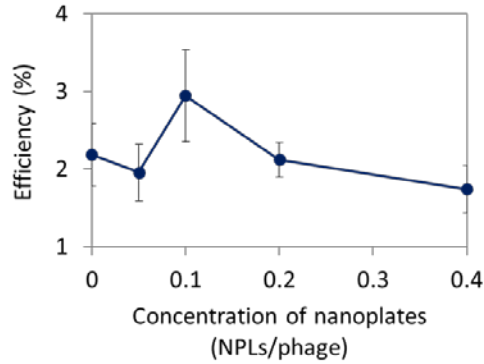


Figure S7. Effect of silver nanoplate concentration on power conversion efficiency in bacteriophage-templated devices. Optimal surface functionalization and biomineralization conditions were used for this study. The highest efficiency is observed for a 0.1 NPL/phage ratio.

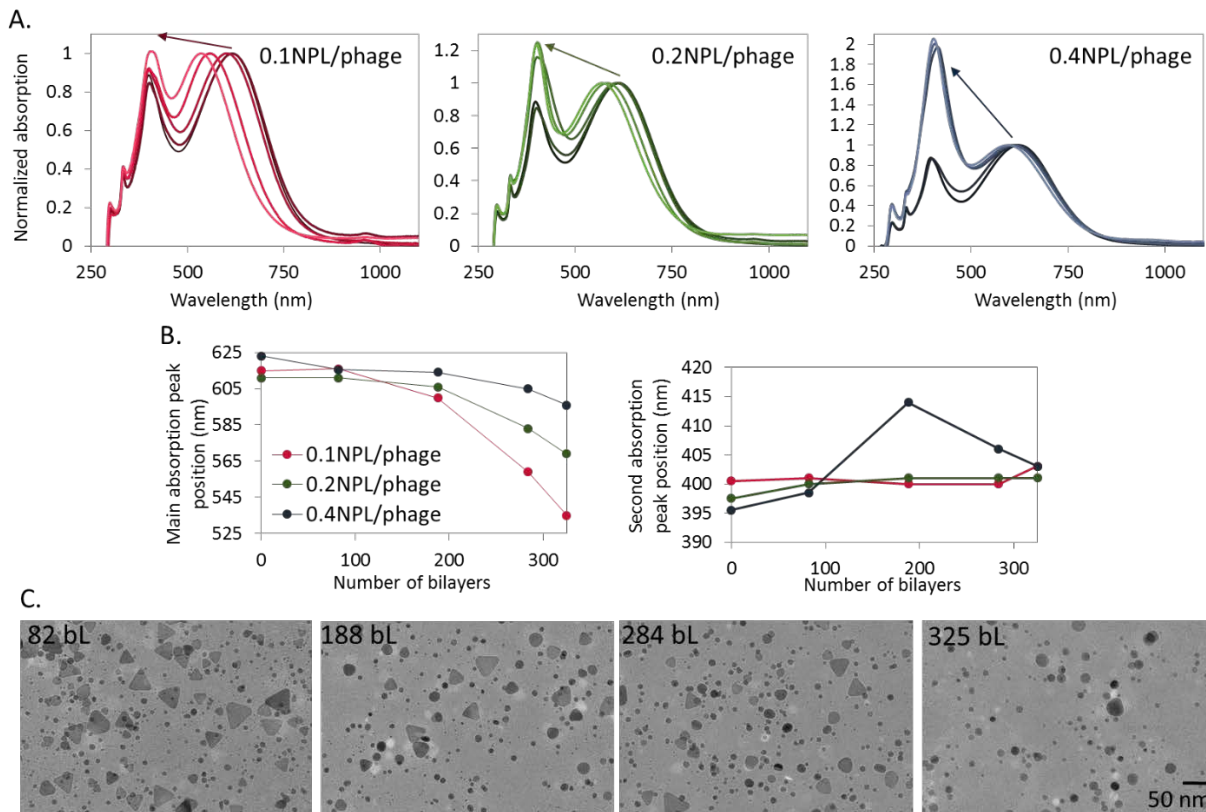


Figure S8. Evolution of the optical properties and morphology of silver nanoplates during the LbL assembly process. Three different ratios of Ag NPLs/phage were used (0.1, 0.2 and 0.4), and the absorption spectra and morphology of the Ag NPL-bacteriophage complexes were monitored initially, and after 82, 188, 284 and 325 bilayers. A. Normalized absorption spectra of Ag NPL-bacteriophage complexes through the process. The spectra are blue shifted as the number of bilayer increases as indicated by the arrows. B. Change in peak positions as a function of the number of bilayers. The peak positioned around 625nm corresponds to the dipole resonance of the NPLs. As the corners of the NPLs become more rounded, this peak shifts towards shorter wavelengths. The 390 nm peak position corresponds to the dipole peak of silver nanospheres. This indicates that during the LbL process the morphology of the NPLs change into spheres or discs as the particles interact with the virus proteins and likely lose the protective citrate ions that preserve the triangular shape. Higher NPL loadings of the virus results in more spheres as indicate by an increase in the 390nm peak, whereas lower loadings result in the NPLs becoming cylindrical discs. C. TEM images showing the morphology of the NPLs as a function of the number of bilayers for 0.4 NPL/phage.

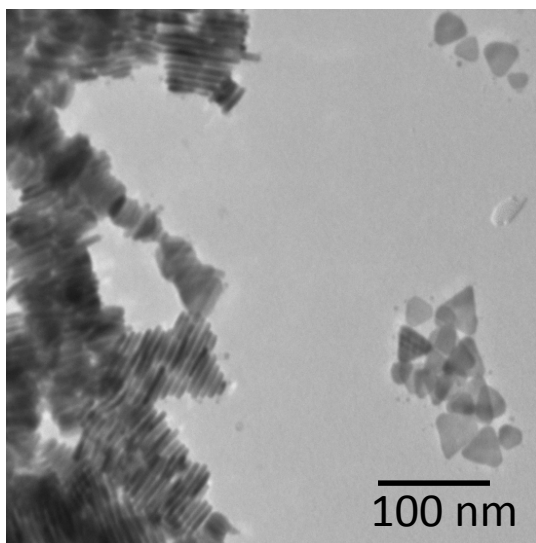


Figure S9. Evidence of Ag NPL stacking, as shown by a TEM image of Ag NPLs dropcast from solution.

Performance of Smaller Area Devices

Figure S10 compares the performance of virus-based devices containing Au NPs with a 0.0547 cm^2 area (as reported throughout this work) and for areas approximately 5 times smaller at 0.0121 cm^2 . Higher currents and fill factors are obtained with smaller area devices. The best small area device reached an efficiency of 4.7 %.

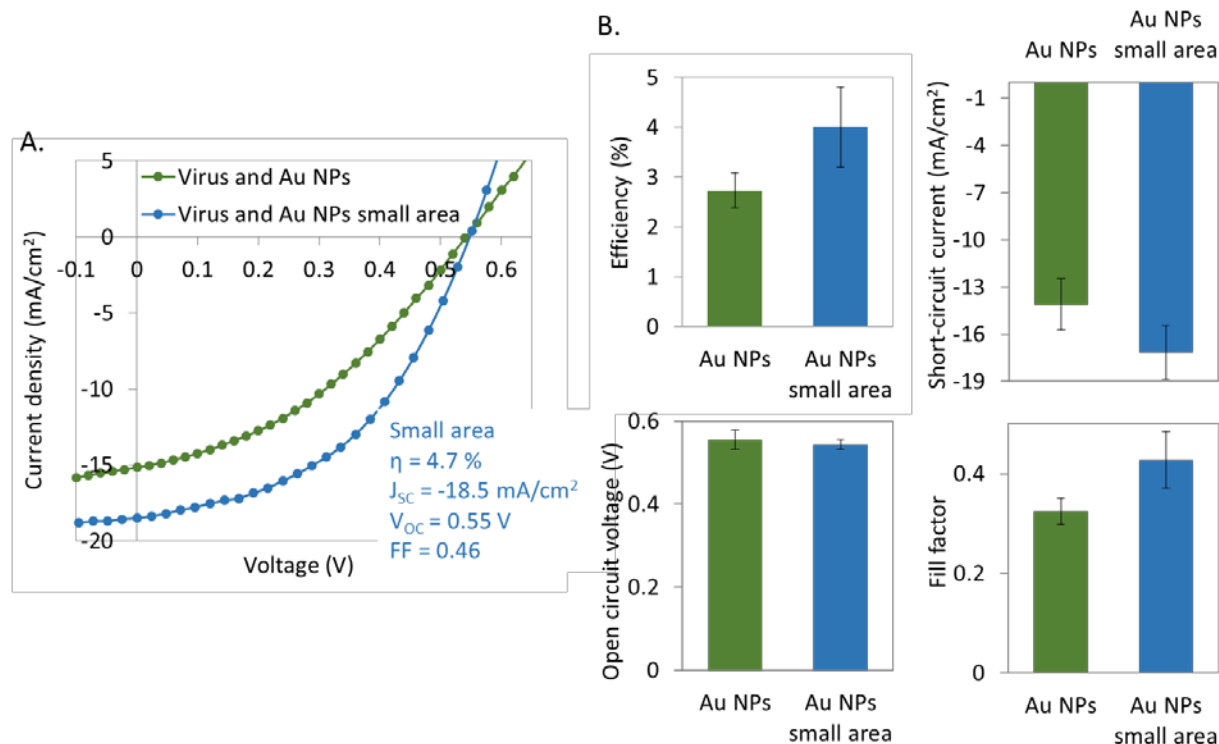


Figure S10. Smaller area devices can reach higher efficiencies. A. Best JV curves and B. Average power conversion efficiency, short-circuit current, open circuit voltage and fill factor, for virus and Au NPs device with areas of 0.0547 cm^2 or 0.0121 cm^2 (small area).

Optical Property Calculations using Effective Medium Theory

Modeling the power absorption throughout the solar cells requires the development of effective complex dielectric functions for the nanostructured active layers of the devices (*i.e.* the virus-templated network infiltrated with PbS QDs, and the PbS QD film layers). Properly modeling the optical material properties is critical for accurately predicting how light propagates and is absorbed throughout the solar cell volume. This section describes the methods used to perform this task.

Pure Anatase Titania

The complex dielectric function for pure anatase titania, ϵ_{TiO_2} , was calculated from the values reported by Kim *et al.*¹ for a 16% porous thin film (84% anatase volume fraction) using Bruggeman effective medium theory:²

$$\epsilon_{TiO_2} = \epsilon_{film} \frac{2 \left(\frac{f_{film} - 1}{f_{film}} \right) \left(\frac{\epsilon_{air} - \epsilon_{film}}{\epsilon_{air} + 2\epsilon_{film}} \right) + 1}{\left(\frac{1 - f_{film}}{f_{film}} \right) \left(\frac{\epsilon_{air} - \epsilon_{film}}{\epsilon_{air} + 2\epsilon_{film}} \right) + 1} \quad (S12)$$

where ϵ_{film} is the complex dielectric function of the 16% porous anatase film reported by Kim *et al.*,¹ f_{film} is the volume fraction of anatase titania in this film (84%), and ϵ_{air} is the dielectric function of air (taken to be 1.000). The complex index of refraction can be calculated from the dielectric function by:

$$n + i\kappa = \sqrt{\epsilon_1 + i\epsilon_2} \quad (S13)$$

where $\epsilon = \epsilon_1 + i\epsilon_2$ is the form of the complex dielectric function, n is the real part of the refractive index, and κ is the imaginary part. The complex index of refraction for pure anatase used for the computations is plotted in Figure S11.

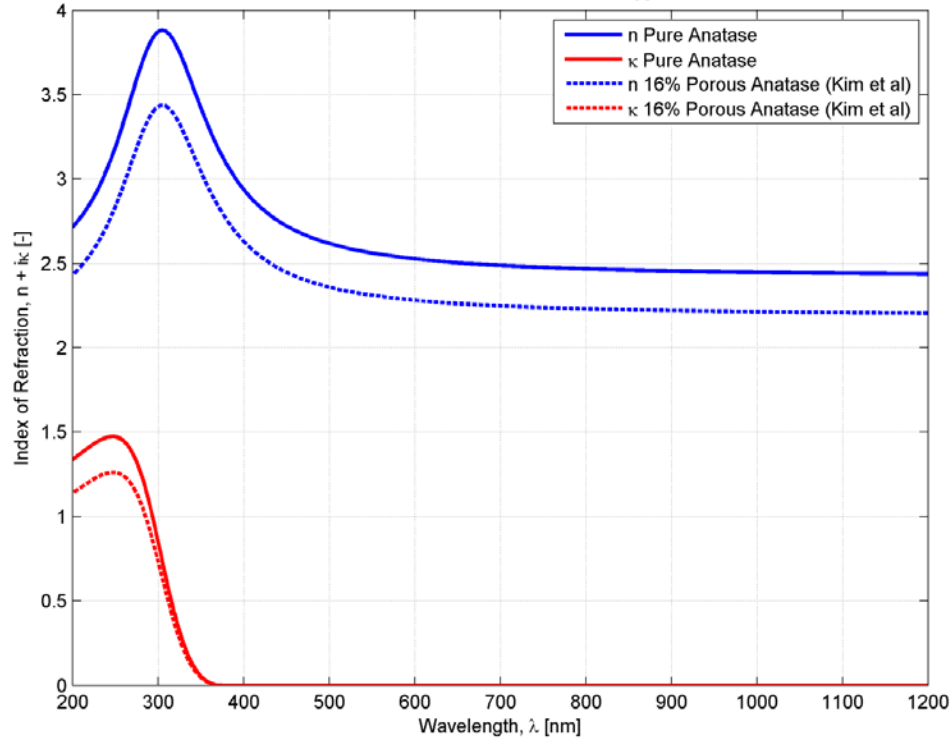


Figure S11. Real (blue) and imaginary (red) components of the index of refraction for the 16% porous anatase TiO_2 film reported by Kim *et al.* (dotted lines) and the estimated function for pure anatase films (*i.e.* 0% porous films, solid lines) as predicted by Bruggeman effective medium theory.

Blend Layer (58% Anatase TiO_2 , 15% PbS QDs, 27% Air)

The complex dielectric function of pure PbS QDs was adjusted from the values reported by Moreels *et al.*³ to have an absorption peak that matches the measurement of 904nm for the PbS QDs used in the devices (see Figure S13).

In reality, a *pure PbS QD* film can never be achieved because void space will always exist between the QDs when the spheres pack into a film. Therefore, effective medium theory must be used to estimate the effective index of the virus-templated titania network when PbS QDs are infiltrated into its pores (referred to as the *blend layer*) and for the packed QD film that was spincoated to form a layer on top of the blend layer (referred to as *random-packed PbS QD layer*). For simplicity the blend layer was model as a homogeneous planar slab with an effective index resulting from a blending of anatase titania (corresponding to virus-templated titania nanowires, comprising 58.1% of the film volume) with the PbS QDs and air occupying the pore space of the

virus-templated network. The volume fraction of PbS in the blend layer was determined to be 15% by averaging the PbS concentration profile reported in Figure 1D of the manuscript over the 50 nm thickness of that film. Although assuming a homogeneous distribution of PbS is a simplification of the system, by using the average PbS concentration measured for the actual films, the total amount of light absorbed by the PbS QDs in the idealized slab will be equal to that absorbed in the actual film. This can be proven using the Beer-Lambert law for light absorption, where light with intensity, I_0 , is incident on a slab with a 1-D concentration gradient, $c(z)$, of PbS QDs with a molar absorptivity of ϵ . The intensity at any position within the slab, $I(z)$, is:

$$I(z) = I_0 \exp\left(\epsilon \int^z c(z) dz\right) \quad (\text{S14})$$

For a slab of thickness L , the intensity of light after passing through the entire film is:

$$I(L) = I_0 \exp\left(\epsilon \int_0^L c(z) dz\right) = I_0 \exp(\epsilon \bar{c} L) \quad (\text{S15})$$

where \bar{c} is the average PbS QD concentration and is equal to:

$$\bar{c} = \frac{1}{L} \int_0^L c(z) dz \quad (\text{S16})$$

A volume fraction of 15% PbS in the blend layer corresponds to a 35% fill fraction of the pores. Therefore, the effective index of the overall blend layer was calculated in two steps. First, the Maxwell Garnett effective medium theory² was used to determine the effective dielectric function of the material in the pores, ϵ_{eff}^{pores} , which is taken to be a 35% fill fraction of PbS QDs with the balance being air:

$$\epsilon_{eff}^{pores} = \epsilon_{air} \left[1 + \frac{3f_{PbS}^{pores} \left(\frac{\epsilon_{PbS} - \epsilon_{air}}{\epsilon_{PbS} + 2\epsilon_{air}} \right)}{1 - f_{PbS}^{pores} \left(\frac{\epsilon_{PbS} - \epsilon_{air}}{\epsilon_{PbS} + 2\epsilon_{air}} \right)} \right] \quad (\text{S17})$$

where ϵ_{PbS} is the dielectric function of pure PbS QDs and f_{PbS}^{pores} is the volumetric fill fraction of PbS QDs in the pore material (35%).

The second step once again uses effective medium theory to blend the anatase titania with the effective medium developed for the pores, ϵ_{eff}^{pores} . The Maxwell Garnett model was not used for this blending because it is only strictly valid for spherical inclusions. Thus, the Bruggeman model was chosen because it applies to a completely randomly inhomogeneous medium. The effective dielectric function of the blend layer, ϵ_{eff}^{blend} , can be found by numerically solving the following transcendental equation:²

$$f_{TiO_2} \frac{\epsilon_{TiO_2} - \epsilon_{eff}^{blend}}{\epsilon_{TiO_2} + 2\epsilon_{eff}^{blend}} + (1 - f_{TiO_2}) \frac{\epsilon_{eff}^{pores} - \epsilon_{eff}^{blend}}{\epsilon_{eff}^{pores} + 2\epsilon_{eff}^{blend}} = 0 \quad (S18)$$

where f_{TiO_2} is the volumetric fill fraction of anatase titania in the blend layer (58.1%) and ϵ_{TiO_2} is the dielectric function of pure anatase titania calculated earlier with Equation S12. Figure S12 plots the real and imaginary parts of the complex refractive indexes calculated for pure anatase, the effective medium in the pores, and the final blend layer comprised of anatase titania, PbS QDs, and air.

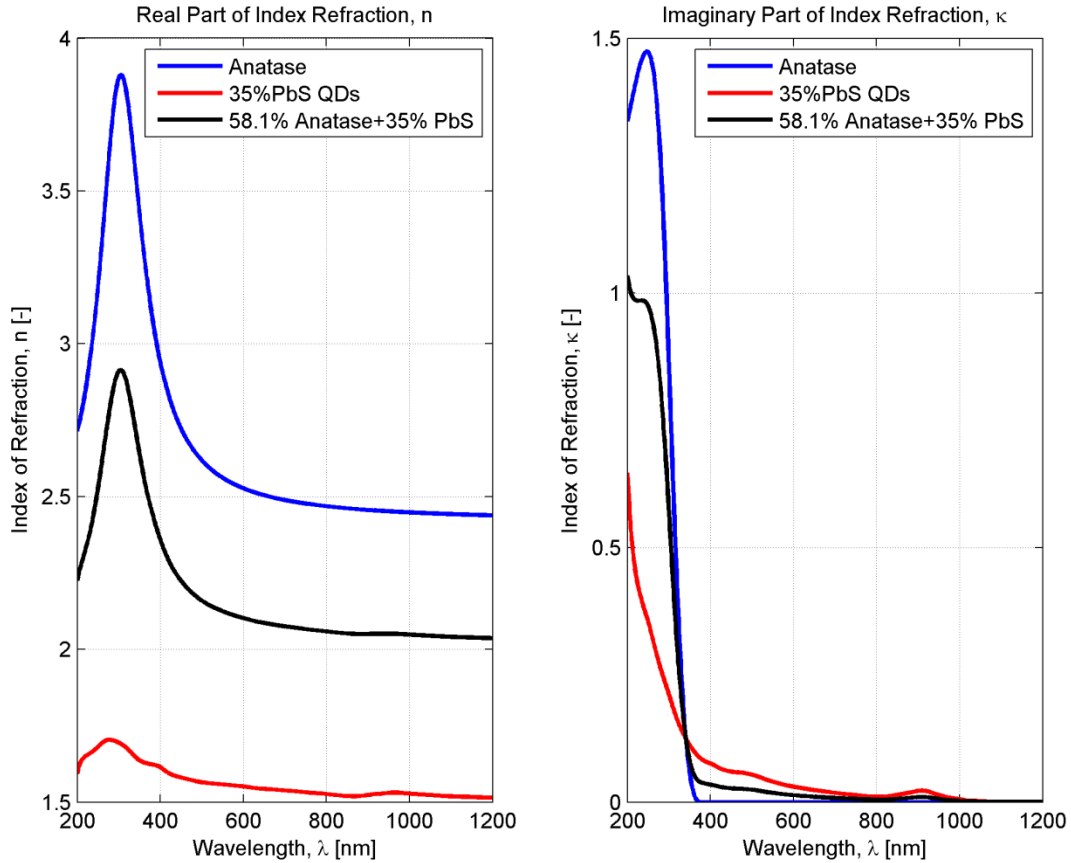


Figure S12. Real (Left) and imaginary (Right) parts of the complex refractive index computed for pure anatase titania (blue lines), the 35% PbS QD 75% air mixture in the pores of the blend layer (red lines), and the final blend layer (black lines) consisting of a 58% volume fraction of anatase titania, 15% PbS QDs, and 27% air.

PbS QD Layer (56% PbS QDs, 44% Air)

When the PbS QD solution is spincoated on top of the blend layer, the nanospheres will pack into a film that consists only of PbS and air. The densest possible packing density for a bed of equal size spheres is 74%, which corresponds to perfect close-packing. In practice, this upper limit is not achieved, rather studies of QD films assembled by spincoating colloidal solutions indicate that packing densities are closer to 50%.⁴ Therefore a PbS volume fraction of 56% was chosen for modeling the spincoated PbS QD film, which corresponds to a typical value used for a loose random-packing of equal spheres.⁵ The effective dielectric function, ϵ_{eff}^{film} , of this layer can be

calculated by using the Maxwell Garnett effective medium model presented in Equation S17, but substituting f_{PbS}^{pores} with f_{PbS}^{film} (56%):

$$\epsilon_{eff}^{film} = \epsilon_{air} \left[1 + \frac{3f_{PbS}^{film} \left(\frac{\epsilon_{PbS} - \epsilon_{air}}{\epsilon_{PbS} + 2\epsilon_{air}} \right)}{1 - f_{PbS}^{film} \left(\frac{\epsilon_{PbS} - \epsilon_{air}}{\epsilon_{PbS} + 2\epsilon_{air}} \right)} \right] \quad (S19)$$

The effective dielectric function resulting from this calculation is plotted in Figure S13.

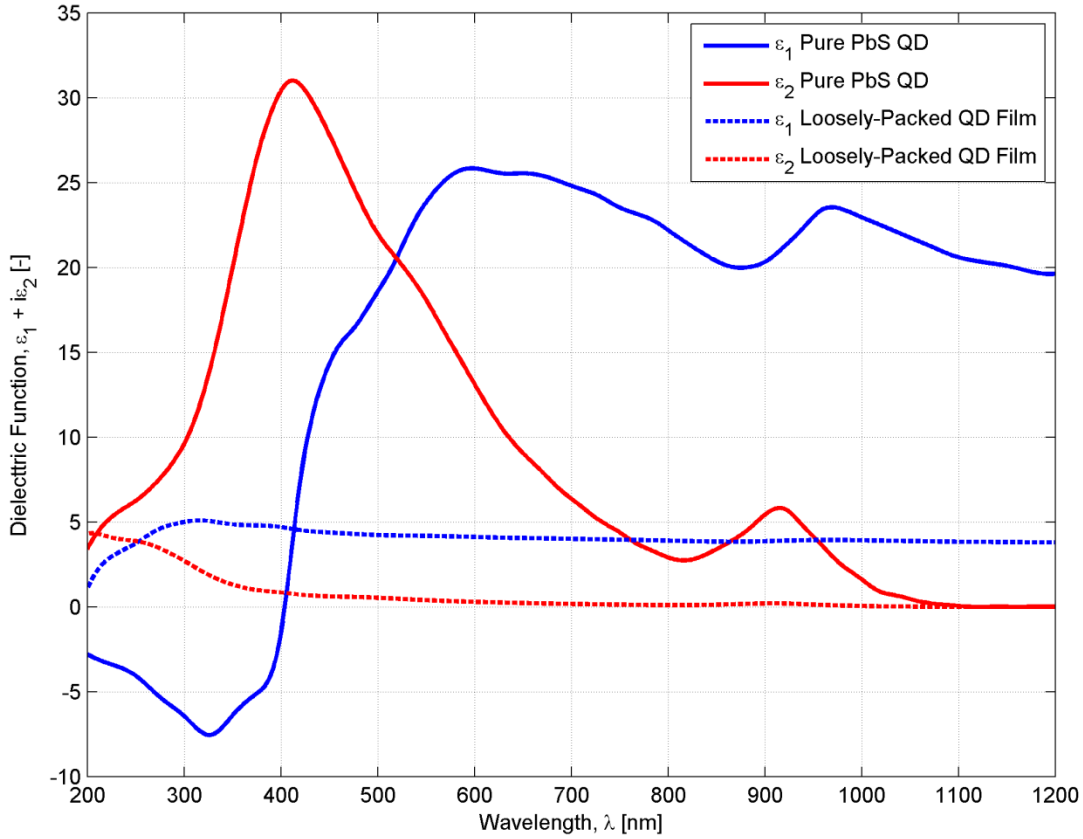


Figure S13. Real (blue) and imaginary (red) components of the complex dielectric function for the pure PbS QDs modified from Moreels *et al.*³ for 904 nm QDs (solid lines) and the estimated effective function for a spincoated film of loosely random-packed PbS QDs (56% volume fraction of PbS QD and 44% air) as predicted by Maxwell Garnett effective medium theory.

FDTD Simulations

In order to computationally predict how a PbS QD solar cell would perform with and without plasmonic metal nanoparticles, the finite-difference time-domain (FDTD) method was used to

determine how light would propagate and become absorbed throughout an idealized device. The simulations were carried out with the software Lumerical FDTD Solutions, Version 8.9.163.

Model Geometry and Materials

The model geometry consists of stacked planar slabs of material starting with 50 nm of FTO at the bottom followed by 100 nm of pure anatase titania, 100 nm of the virus-templated blend layer that has been infiltrated with PbS QDs (58% volume fraction of TiO₂, 15% PbS, 27% Air), 100 nm of PbS QD film (56% PbS, 44% Air), and 25 nm of MoO₃ on top. The complex dielectric functions developed for pure anatase titania, the virus-built titania-PbS QD blend layer, and the random-packed QD film layers using effective medium theory in the previous section were assigned to the corresponding slabs of the model geometry. The lateral extent of the slabs in the x - and y -directions was fixed to be 60 nm, which is the estimated approximate distance between NPs in the solar cells. Three different types of nanoparticles were considered in the plasmon-enhanced solar cells: gold nanosphere (Au NP), silver nanosphere (Ag NP), and silver nanoplate (Ag NPL). The radius of the nanospheres was taken to be 10 nm whereas the cylindrical silver nanoplates had a radius of 10 nm and a thickness of 6 nm. The complex dielectric function reported by Johnson and Christy⁶ was used for gold, whereas the function reported by Palik⁷ was used for silver. Periodic boundary conditions were placed on each of the lateral x - and y - faces of the model in order to simulate an infinite slab with periodically spaced NPs. Likewise, this allows any light that is scattered obliquely from a NP through the lateral faces to re-enter the simulation volume. Six different configurations were performed for each nanoparticle type, each with the nanoparticle positioned at a different location throughout the thickness of the active materials. Because the nanoparticles were built into the blend layer using the layer-by-layer assembly method with the M13 virus, the NPs can be located anywhere within this layer. Five configurations consider a nanoparticle located within the blend layer (10, 30, 50, 70, or 90 nm from the bottom of the blend layer slab). However, in an actual device, the interfaces between the blend and random-packed QD layers is not expected to be smooth, rather the virus-templated titania nanowire film is expected to be rough. Therefore, a NP that exists near the top of the film could almost be considered to be embedded within the random-packed QD film layer. Thus, a sixth configuration was considered where the metal NP was located 10

nm into the random-packed QD film layer. Because the Ag NPL is not spherically symmetric, its orientation to the incident light will impact the nature of its plasmon resonance; thus, for each vertical position, three separate orientations were considered with the NPL located at 0° , 45° , and 90° to the incident field (*i.e.* 18 total cases were considered for the Ag NPL geometry and 6 cases for the Au NPs and Ag NPs.).

The model geometry was illuminated from the FTO side with a plane-wave source at 400 different wavelengths between 200 and 1200 nm to fully capture the incident solar spectrum of interest. All simulations were performed with a refined mesh size of 1 nm in the region around the metal NP and used conformal meshing option “Conformal Variant 1” to provide greater accuracy in elements where multiple materials are present. A three-dimensional power absorption monitor was placed throughout the active regions of the solar cell to capture how much power was absorbed at each point in the solar cell. A cross-section of the mesh through the NP center is shown in Figure S9A for the nanosphere case and Figure S14B shows the mesh configuration for all three orientations of the nanoplate cases.

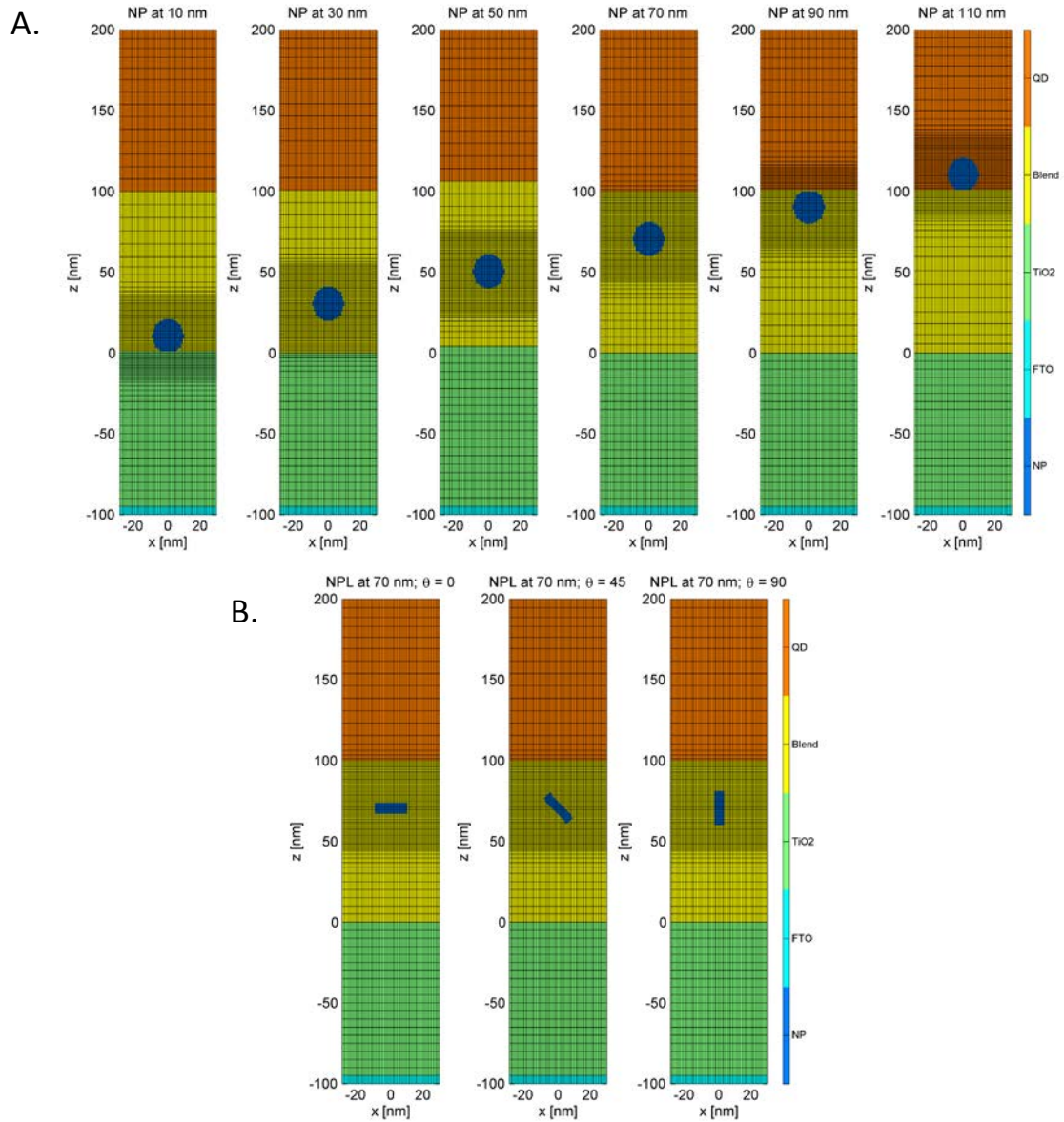


Figure S14. The mesh, materials, and geometry of each simulated configuration performed with the FDTD method. A. All six of the different positional configurations of metal NPs. Five configurations exist for a NP within the blend layer and 1 in the random-packed PbS QD film layer. B. Because silver nanoplates are not spherically symmetric, their orientation within the blend layer will change the way light is concentrated in the near-field surrounding them. Therefore, at each of the six positional configurations shown in A, three orientational configurations were considered with the NPL positioned at 0° , 45° , and 90° with respect to the faces of the material slabs (18 total cases performed for the NPL device).

As discussed in the manuscript, the silver nanoplates are believed to transform into a polydisperse population of silver nanospheres during the annealing process the virus-templated titania film undergoes to convert the nanowires from amorphous to crystalline titania. The simulations performed to test this hypothesis are exactly the same as those done for the Ag NPs except that nanospheres of radius 8.2, 10.4, and 11.9 nm were considered, which conserve the volume of a stack of 1, 2, and 3 NPLs.

Calculating Power Absorption, External Quantum Efficiency, and Photocurrent Enhancement

Upon completion of the simulation, the power absorption monitor provides the source-normalized power density that has been absorbed at each node throughout the mesh for each illumination wavelength. This can be thought of as a measure of *absorption efficiency density*, p_{abs} , which is how efficiently a given element can absorb photons of a particular wavelength that are incident upon the solar cell per unit volume (units of m^{-3}). By integrating this measure over the spatial extent of active regions in the solar cell, the total absorption efficiency of the solar cell can be determined as a function of wavelength. It must be noted that when metal NPs are incorporated into the model, any light that is absorbed in the NP interior cannot contribute to enhancing solar cell performance because the power it absorbs either goes into producing the near-field or is lost as heat. Only the light that is concentrated by the LSPR of the NP in the active material directly surrounding it can contribute to photocurrent enhancement. Therefore, when determining the total amount of power absorbed by the solar cell with the goal being to estimate the photocurrent the device can produce, only the power absorbed in the active media should be considered. The external quantum efficiency, EQE , of the solar cell, which quantifies how many photons of a given wavelength incident on the solar cell are converted into collected charges, can be estimated by:

$$EQE(\lambda) = \eta_c \eta_a(\lambda)(1 - R(\lambda)) \quad (\text{S20})$$

where η_a is the absorption efficiency, η_c is the charge collection efficiency, and R is the reflectance of the solar cell. For simplicity the following assumptions are made in the solar cell.

1. It is assumed that none of the incident light is reflected: $R = 0$.
2. It is assumed that the PbS QDs in the blend layer are fully depleted by the nanoporous virus-templated titania film. Therefore, any carriers generated within the blend layers will be efficiently transported by drift due to the built-in field in this region. This, it is assumed $\eta_c = 1$ within the blend layer.
3. For simplicity, it is assumed that the depletion region only encompasses the blend layer and does not extend in to the random-packed QD layer above. The basis of this assumption is that there are less quantum dots and titania present in this layer than in a bilayer geometry, which causes the depletion width to be shorter than the typical value of ~ 150 nm. Therefore, the random-packed QD layer is assumed to be within the quasi-neutral region of the heterojunction where diffusion governs charge extraction. Therefore, electrons that are generated deeper in the PbS QD film above the blend layer are less likely to diffuse to the depletion region for efficient collection. To capture this effect, an exponential decay envelop with a decay length of 30 nm, corresponding to the diffusion length of electrons in the PbS QD film, is used for the charge collection efficiency in the random-packed PbS QD film layer. Therefore:

$$\eta_c(z) = \begin{cases} 1, & 0 \leq z \leq L_b \\ e^{-(z-L_b)/L_d}, & L_b < z \leq L_b + L_{QD} \end{cases} \quad (\text{S21})$$

where L_b is the thickness of the titania-PbS QD blend layer, L_{QD} is the thickness of the close-packed QD layer, and L_d is the decay length (*i.e.* 30 nm).

The absorption efficiency, η_a , is determined by integrating the absorption efficiency density, p_{abs} , over the volume of the active layers:

$$\eta_a(\lambda) = \int_{\substack{\text{Active} \\ \text{Material} \\ \text{Volume}}} p_{abs}(x, y, z, \lambda) dx^3 \quad (\text{S22})$$

The EQE can be estimated from the FDTD simulations by multiplying the normalized power absorption density provided by the 3D power monitor, *i.e.* p_{abs} , by the η_c given in Equation S21,

and integrating over the volume of the active layer that contains the blend material or the random-packed PbS QD layer active materials (we exclude the power absorbed in the metal NP volume from consideration):

$$EQE(\lambda) = \int_{\substack{\text{Active} \\ \text{Material} \\ \text{Volume}}} \eta_c(z) p_{abs}(x, y, z, \lambda) dx^3 \quad (S23)$$

To account for the different geometrical configurations that the NP and NPL can have in the actual devices, the simulated EQE reported in the manuscript is the ensemble average over all of the cases considered for that device type (*i.e.* 6 cases for No NPs, Au NPs, and Ag NPs; 18 cases for Ag NPLs). For the corrected Ag NPL predictions, which instead simulate three differently sized nanospheres, a total of 18 cases are considered and the ensemble average is taken over this set.

Once the ensemble average quantum efficiency has been determined, the photocurrent enhancement for a given device type (*i.e.* no NPs, Au NPs, Ag NPs, Ag NPLs) can be calculated by comparing the estimated short circuit photocurrent densities of the devices with metal NPs to that without. The short circuit current density can be predicted by:

$$J_{sc} = q \int_{\lambda_{min}}^{\lambda_{max}} EQE(\lambda) b_s(\lambda) d\lambda = \frac{q}{hc} \int_{\lambda_{min}}^{\lambda_{max}} EQE(\lambda) M(\lambda) \lambda d\lambda \quad (S24)$$

where q is the charge on an electron, b_s is the photon flux of the AM 1.5 solar spectrum, M is the spectral irradiance of the solar spectrum (which can be related to b_s by: $M(\lambda) = \frac{b_s(\lambda)}{E(\lambda)} = \frac{\lambda b_s(\lambda)}{hc}$), h is Planck's constant, c is the speed of light, and $\lambda_{min} = 200$ nm and $\lambda_{max} = 1200$ nm for the simulations.

Therefore, the photocurrent enhancement factor, EF , is defined to compare the photocurrent produced in the plasmonic devices to that generated in the same device without metal NPs:

$$EF = \frac{J_{Sc}^{NP}}{J_{Sc}^{No NP}} = \frac{\int_{\lambda_{min}}^{\lambda_{max}} EQE_{NP}(\lambda)\lambda M(\lambda)d\lambda}{\int_{\lambda_{min}}^{\lambda_{max}} EQE_{No NP}(\lambda)\lambda M(\lambda)d\lambda} \quad (S25)$$

Calculating Plasmon Decay Length

The distance over which the near-field generated by the metal nanoparticles via LSPR can penetrate into the surrounding active media was determined by analyzing line profiles of the absorbed power density taken through the center of the NP while at resonance. The resonance wavelength was determined as the simulated illumination wavelength that produced the largest absorbed power value outside the metal NP core. Figure S15 shows a contour plot of the absorbed power density of each NP device case at resonance taken through the center plane of the metal NP.

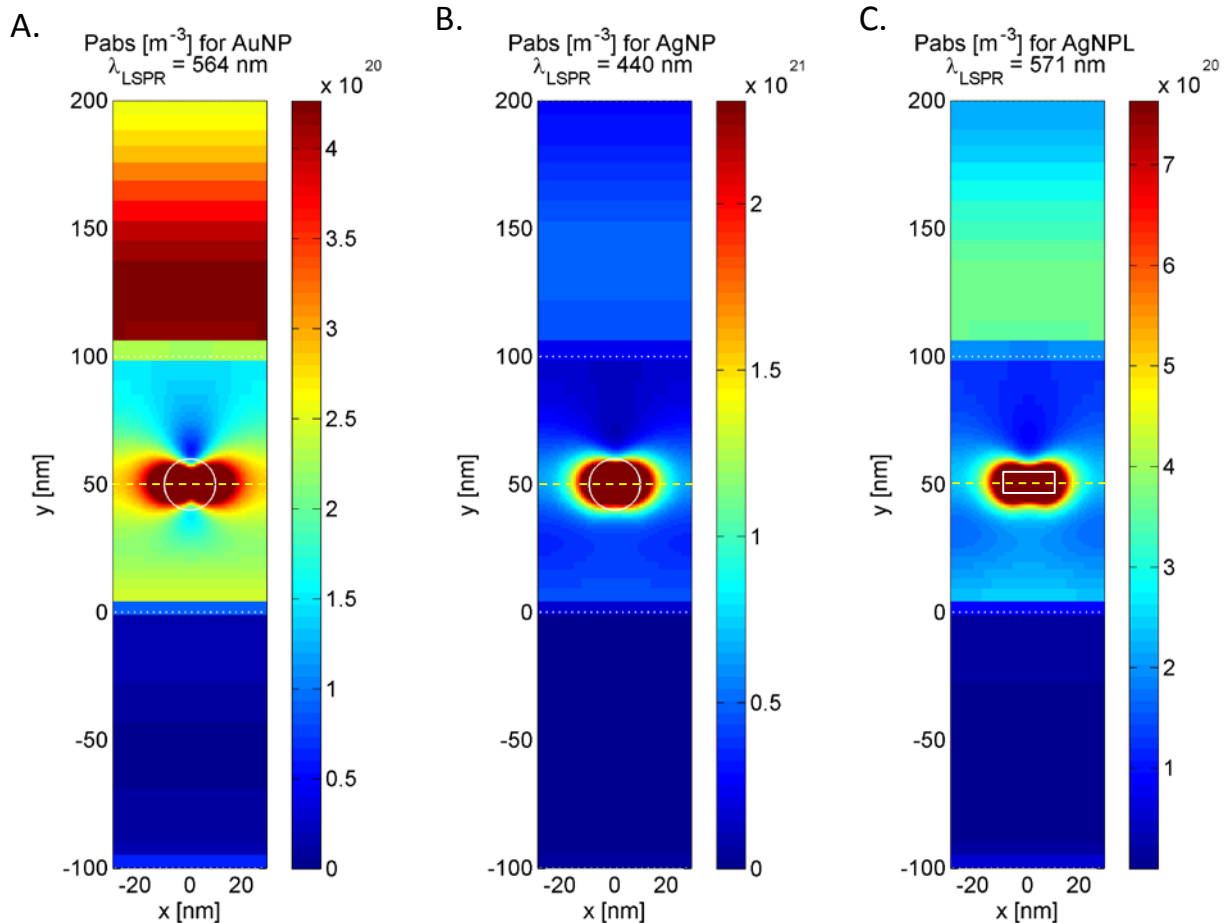


Figure S15. Contour plots of source-normalized absorbed power density, p_{abs} [m^{-3}], throughout the simulated solar cell cross-section at a plane through the center of the A. Au NP at $\lambda=564$ nm, B. Ag NP at $\lambda=440$ nm, and (C) Ag NPL at $\lambda=571$ nm. The dotted yellow line indicates the position where the line profiles are taken to determine the plasmon decay length.

The influence of illumination wavelength on the penetration length of the near-field generated by the metal NP into the active media was investigated by sampling the absorbed power density along a line through the center of the metal NP (indicated by the yellow dotted line in Figure S15). Figure S16 plots this line profile for every simulated wavelength for all three NP types. It can be observed that although plasmon resonance increases the absorbed power most strongly at the LSPR wavelength, enhancement occurs over a spectral range of about 100 nm for the nanospheres and 200 nm for the nanoplate cases. It should also be noted that the spatially flat

absorption line around wavelength 350 nm corresponds to the main absorption peak of the PbS QD rather than plasmon resonance of the metal NP.

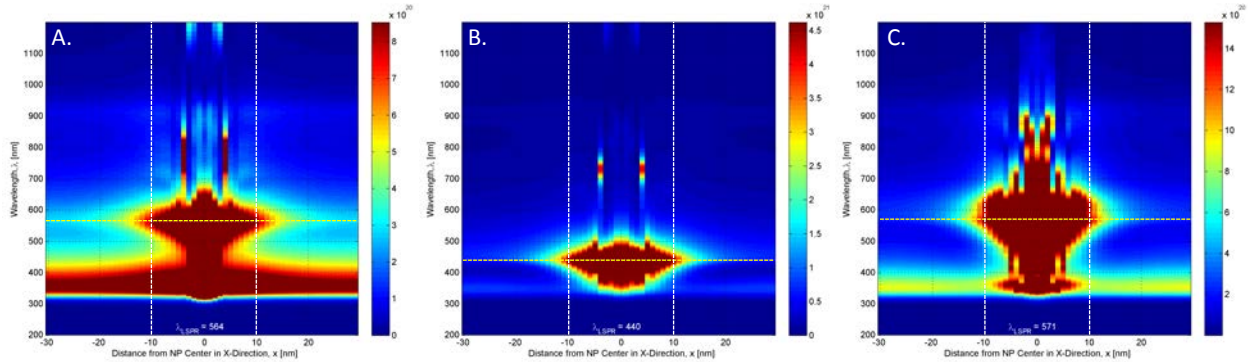


Figure S16. Line profile plots of source-normalized power density, p_{abs} , as a function illumination wavelength for A. Au NP, B. Ag NP, and C. Ag NPL (horizontal configuration). The dotted horizontal yellow line indicates the LSPR wavelength and the dotted vertical white lines indicate the edges of the metal NP. The area between the dotted white lines represents the power absorbed in the interior of the metal NP, whereas the area outside represents the power absorbed in the blend layer of the solar cell.

In addition to performing simulations with the metal NPs located within the blend layer, simulations were also performed with the metal NPs located within the random-packed PbS QD film layer in the absence of the blend layer (device structure: FTO (50nm)\Random-Packed PbS QD Layer (100 nm)\MoO₃). Figure S17 shows the power absorption density line profiles through the NP centers at the LSPR resonance peak and normalized to the maximum value within the active medium for each NP type embedded in both the blend (Figure S17A) and random-packed PbS QD layer (Figure S17B). The dotted line indicates that location where the normalized value reaches $1/e$, which corresponds to the decay length.

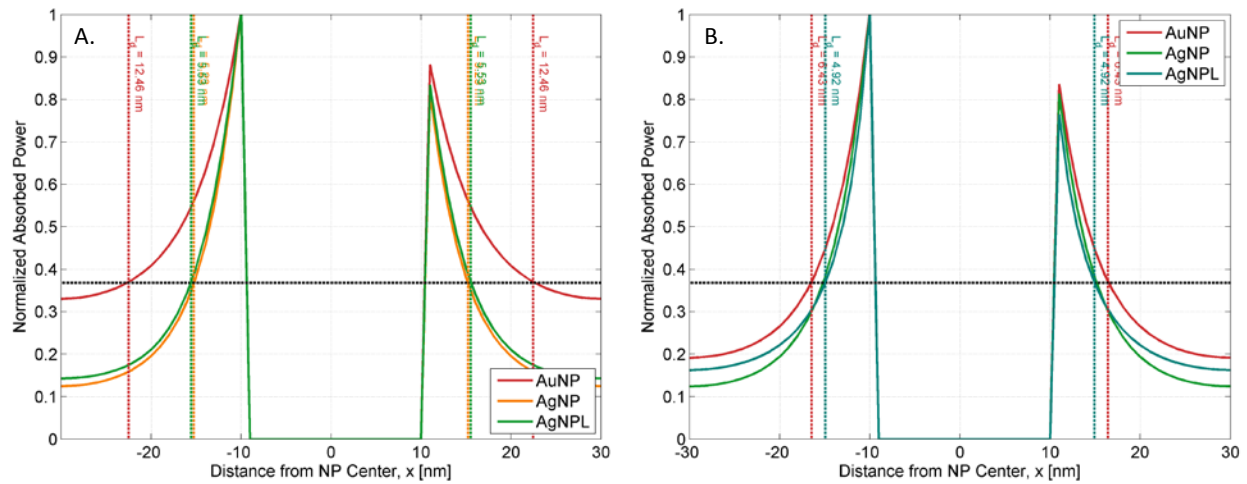


Figure S17. Line profile plots of absorbed power density normalized to the maximum value outside of the metal NP core for each of the NP types at the LSPR wavelength. The decay profile for the metal NPs embedded in the blend layer is shown in part A. Part B. shows the decay profiles when the metal NPs are embedded in the random-packed PbS QD layer of a device without the blend layer (a simple bilayer). The horizontal dotted black line represents the value $1/e$, which corresponds to the decay length, indicated by the vertical dotted lines. The printed value L_d is the decay length, *i.e.* the distance from the NP surface when a normalized value of $1/e$ is reached. Note that profiles appear slightly asymmetric due to the way the simulation domain was meshed.

Fitting Measured JV Curves to Standard Solar Cell Model

It was hypothesized that the reason the solar cells with plasmonic NPs produced an increased open-circuit voltage, V_{oc} , was simply a natural result of the solar cells producing a higher photocurrent. The intuition behind this notion is that the standard diode model of solar cells couples together the bias voltage and the photocurrent. Therefore, it would be expected that if the same device would somehow generate a higher current (for instance due to improved light harvesting by LSPR), then the open-circuit voltage would also increase accordingly. Figure 5E in the manuscript shows that the measured JV curves of the virus-based solar cell without NPs has a similar shape to that of the virus-based solar cell that has been assembled with Ag NPLs, and one could imagine that the curve for the Ag NPL device might be almost reproduced if the virus-only curve was translated along the y-axis to match the short-circuit current values. This hypothesis

was tested by fitting the measured JV data to the standard diode equation for solar cells that includes parasitic resistances:

$$J = J_{sc} - J_0 \exp\left(\frac{q(V + JAR_{sr})}{mkT}\right) - \frac{V + JAR_{sr}}{R_{sh}} \quad (\text{S26})$$

where J is the current density, J_{sc} and J_0 are the short-circuit current densities for the light and dark current, respectively, q is the charge on an electron, V is the applied voltage bias, m is the ideality factor (which is a function of bias, V), k is Boltzmann's constant, T is device temperature (assumed to be room temperature, 298 K), R_{sr} is the series resistance, R_{sh} is the shunt resistance, and A is the illuminated area of the device.

The series and shunt resistances were determined by calculating the inverse of the slope of the measured JV curves near the x -intercept and y -intercept, respectively. Likewise, the dark and light short-circuit current densities were determined from the measured light and dark JV curves for each of the devices by finding the current density when the applied bias voltage is equal to zero.

The ideality factor, m , characterizes how far the actual solar cell behavior deviates from an ideal diode ($m = 1$) while under illumination. This factor was determined for each applied bias by rearranging Equation S25:

$$m(V) = \frac{q(V + JAR_{sr})}{kT} \left[\ln \left(\frac{J_{sc} - J - \frac{V + JAR_{sr}}{R_{sh}}}{J_0} \right) \right]^{-1} \quad (\text{S27})$$

The calculated ideality factor for illuminated devices are plotted in Figure S18 for the devices made from TiO_2 paste (no virus), the virus-film device without metal NPs, and the virus-film device with Ag NPLs.

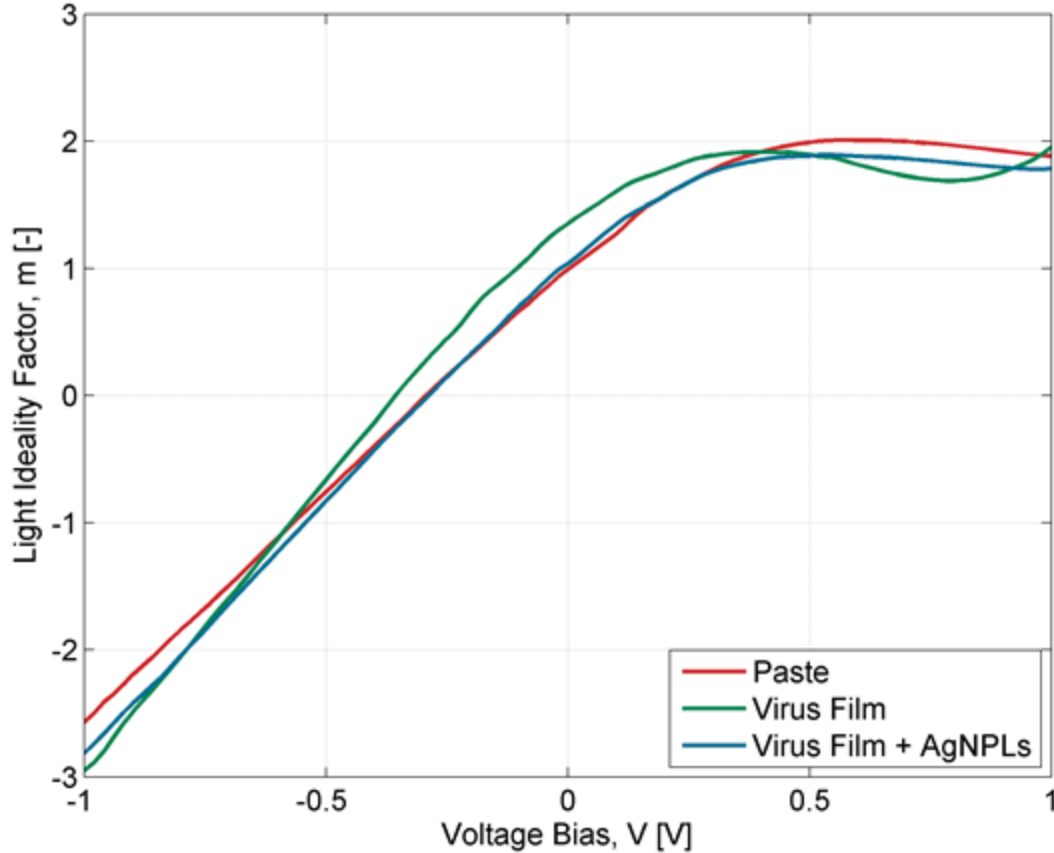


Figure S18. The ideality factor as a function of applied voltage bias, as determined from the measured JV curves while illuminated (*i.e.* the *light ideality factor*).

The advantage of the standard model described by Equation S25 is that every term represents a physical characteristic of the solar cell. Thus, changes in solar cell performance can be predicted by adjusting some of these terms and solving the equation. Now that the parasitic resistances and the ideality factor have been determined from the measured light JV curves, it can be predicted how a given device would perform if it were able to somehow generate a different photocurrent. By taking the values for R_{sr} , R_{sh} , and $m(V)$ determined for the *virus-film solar cell without plasmonic nanoparticles* and plugging them into the standard model (Equation S25), but now substituting the J_{sc} and J_0 values measured for the *virus-film solar cell with Ag NPLs*, the JV curve can be predicted for how the non-plasmonic virus-based solar cell would perform if it could suddenly generate the current measured in the virus-based device with Ag NPLs. This was accomplished by numerically solving the transcendental Equation S25 with these values; the result is plotted in Figure S19. The fact that the predicted V_{oc} is so close to that measured for the

virus-based device with Ag NPLs strongly indicates that the increase in open-circuit voltage shown by the plasmonic solar cells is a natural result of the increase in photocurrent that results from the improved light harvesting in the device via LSPR by the metal NPs. It could be argued that any difference between the measured curve for the *virus-based device with Ag NPLs* and the curve predicted from the *non-plasmonic virus solar cell* is due to slight variations in the device morphologies that produce slightly different series and shunt resistances.

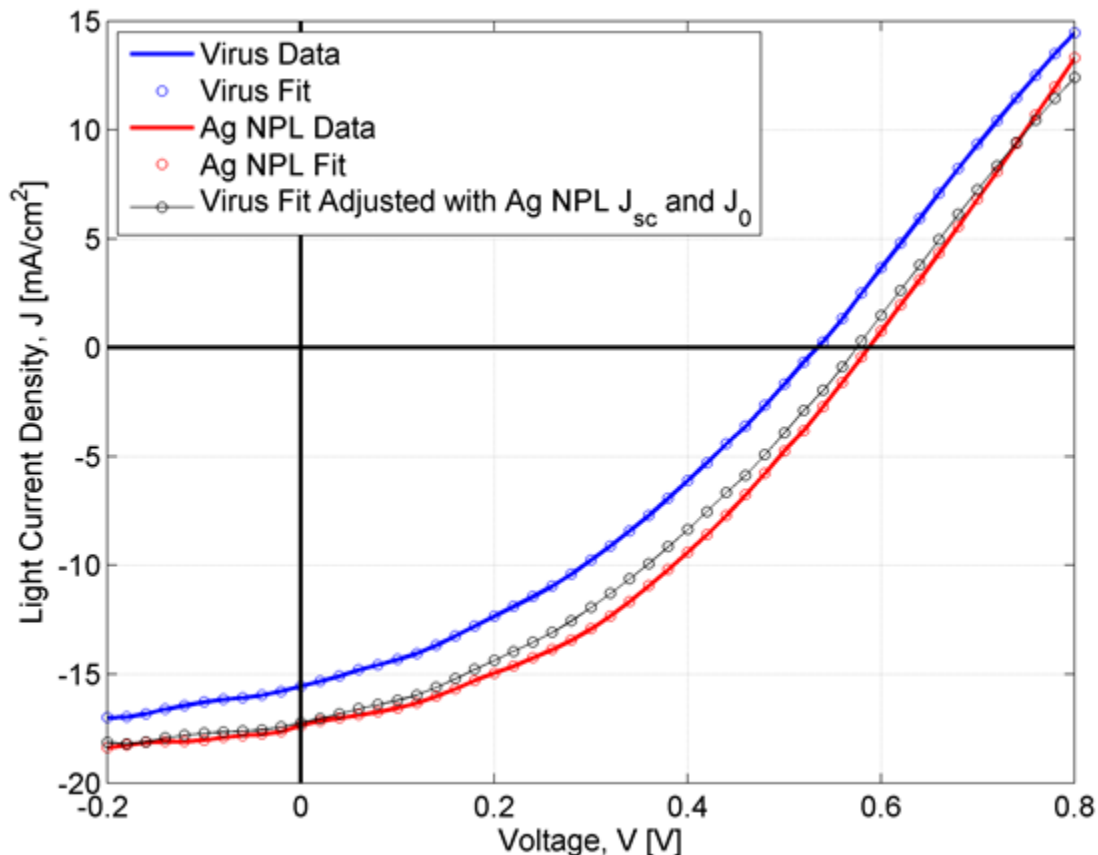


Figure S19. The measured light JV curves for the *virus-film solar cell without plasmonic NPs* (solid blue line) and the *virus-film solar cell with Ag NPLs* (solid red line), with the open circles indicating the predicted curve that has been fit to the standard solar cell equation given in Equation S25. The black line represents the predicted JV curve from Equation S25 of the *non-plasmonic virus-film solar cell* (solid blue line) if it generated the short-circuit photocurrent produced by the virus-based device with Ag NPLs.

Materials and Methods

Materials

1-octadecene (technical grade, 90 %) (ODE), oleic acid (technical grade, 90 %) (OA), lead (II) oxide (technical grade, 99.999 %), cadmium chloride (99.99 %), hexamethyldisilathiane (synthesis grade) (TMS-S), titanium tetrachloride, (3-aminopropyl)trimethoxysilane (APTMS), 1-Ethyl-3-(3-dimethylaminopropyl)carbodiimide (EDC), gold(III) chloride ($\geq 99.99\%$ trace metal basis), silver nitrate, coumalic acid, hydrogen peroxide (Perdrogen, 30% solution), sodium borohydride, glycerol, and branched PEI (1.3kDa) were purchased from Sigma (St-Louis, MO). 1-tetradecylphosphonic acid (98%) (TDPA) and sodium citrate dihydrate were purchased from Alfa Aesar (Ward Hill, MA). Oleylamine (80-90 %) was purchased from Acros (Fair Lawn, NJ). N-hydroxysulfosuccinimide (sulfo-NHS) was purchased from Pierce Biotechnology Inc. (Rockford, IL). TEC 15 FTO-coated glass substrates were purchased from Pilkington Glass (Northwood, OH). Polyallylamine hydrochloride (PAH, 120000 to 200000 g mol⁻¹) and polyacrylic acid (PAA, >250000 g mol⁻¹) were purchased from Polysciences Inc. (Warrington, PA). Titania paste (HT/SC, 8-10 nm particles) was purchased from Solaronix SA (Switzerland).

M13 Bacteriophage

The E3 M13 bacteriophage variant was amplified by infecting exponentially growing *Escherichia coli* bacteria. The bacteriophage was separated from cell debris via centrifugation and further purified with two cycles of polyethylene glycol-sodium chloride precipitation and centrifugation. The final product was diluted in a PBS buffer, and the EEE peptide displayed on each pVIII protein was confirmed with DNA sequencing.

For metal nanoparticle binding, the p8#9 variant was used, and amplified as described above. The VSGSSPDS peptide displayed on the pVIII proteins was confirmed with DNA sequencing.

Gold Nanoparticle (Au NP) Synthesis

Gold nanoparticles with ~20 nm diameters were synthesized following the Turkevich method.⁸ In summary, 95 mL of deionized water and 2.6 mL of 50 mM gold(III) chloride were combined in a 250 mL round-bottom flask and brought to a boil while stirring in a silicone oil bath. While boiling, 10 mL of 1% wt sodium citrate dihydrate was quickly added while vigorously stirring. The color of the solution quickly turned black and then ripened into a deep ruby red. The solution was kept boiling and stirring for an additional 20 minutes. The solution was cooled to room temperature and stored without further purification.

Silver Nanoparticle (Ag NP) Synthesis

Silver nanoparticles were synthesized following a modified Turkevich method.⁸ In summary, 95 mL of deionized water and 4 mL of 30 mM silver nitrate were combined in a 250 mL round-bottom flask and brought to a boil while stirring in a silicone oil bath. While boiling, 10 mL of 5% wt sodium citrate dihydrate was quickly added while vigorously stirring. After stirring for a minute, 6 mL of 100 mM coumalic acid was quickly added. The color of the solution slowly ripened into a deep yellow-brown color. The solution was kept boiling and stirring for an additional 20 minutes. The solution was cooled to room temperature and stored without further purification.

Silver Triangular Nanoplate (Ag NPL) Synthesis

Silver nanoparticles were synthesized by modifying the method previously reported by Zhang *et al.*⁹ In a 1 L Erlenmeyer flask, 240 mL of deionized water was combined with 5 mL 50 mM silver nitrate and 5 mL 750 mM sodium citrate dihydrate while stirring at room-temperature, followed by 6 mL of 30% hydrogen peroxide stock solution. While stirring at room-temperature, 10 mL of freshly prepared 100 mM sodium borohydride was added dropwise to the solution. The color of the solution should change from yellow to brown to amber-red within about fifteen minutes. Once the color has stabilized, add 3 mL of 30% hydrogen peroxide solution. Repeat addition of hydrogen peroxide, if necessary, until the solution has changed color and stabilized to a deep blue. Add 1 mL of glycerol to stabilize the solution for long-term storage.

PbS Quantum Dot Synthesis

PbS quantum (QD) synthesis followed previously published methods.^{10 11} A metal halide precursor was first prepared by dissolving 0.3 g CdCl₂ and 0.033 g of TDPA in 5 mL of oleylamine in a three-neck flask and degassed at 100 °C under vacuum. The metal halide solution was then kept at 80 °C under nitrogen.

In a separate three-neck flask, 0.45 g of PbO, 1.5mL of oleic acid, and 18 mL of ODE were degassed under vacuum at 125 °C. A sulfur precursor was prepared by mixing 0.18g of TMS-S (weighed out in an argon atmosphere glovebox) with 10mL of degassed ODE. The sulfur precursor solution was then rapidly injected into the reaction flask at 125 °C. Immediately after injection, the reaction mixture was removed from heat and allowed to cool down to room temperature. When the mixture cooled down to 60-70 °C, 1 mL of the metal halide precursor solution was rapidly injected. Once the entire mixture reached room temperature, the QDs were purified and isolated through several centrifugation wash cycles. The QDs were first precipitated with acetone and isolated by centrifugation. The QDs were subsequently re-dispersed in toluene and precipitated again with excess acetone and methanol, followed by centrifugation. Finally, the QDs were washed several more times with methanol and stored as a dry powder.

Device Assembly

Patterned FTO substrates were cleaned sequentially in soap, water, acetone and isopropanol with sonication. After drying with N₂ gas, the substrates were plasma treated for 2 min, and a base layer of titania paste (Solaronix, HT/SC) was spun at 2000 rpm and annealed at 500 °C for 1 h.

The titania paste layer was functionalized either with aminopropylsilanetriol and by attaching a first layer of viruses with EDC as previously described,¹² or by functionalizing the surface either with 4.5 bilayers of PAH/PAA or with a branched PEI (1.3kDa) spincoated at 0.1 w% in water at 5000 rpm, and electrostatically adsorbing the first layer of viruses in a NaOAc buffer (pH 4.9) at 50 °C for 45 min. After each functionalization, the films were rinsed with milli-Q water and dried with N₂ gas. Virus films were assembled via covalent layer-by-layer, as described previously.¹² To remove any residual salts or organics, the films were rinse in milli-Q water for at least 30 min after LbL.

Titania was nucleated onto the virus films using a 0.2 M TiCl_4 solution in water. The hydrolysis occurred at 80 °C for 1.5, 2 or 2.5 h. The films were then sonicated for a few seconds in milli-Q water, and rinsed for at least 30 min. The titania-coated virus films were annealed at 500 °C for 1h.

Oleic acid-capped PbS QDs at 50 mg/mL in octane were dropped onto the titania films for 1 min, and then spun at 2500 rpm for 10 s. Ligand exchange was performed with MPA (1 % in methanol), which was spun for 10s, then rinsed with methanol and spun for 10s, and rinsed with octane and spun for 10s. The cycle was repeated a total of five times.

Patterned electrodes of MoO_x (25 nm) and Au (100 nm) were thermally evaporated onto the PbS film. The resulting area of each device was 0.0547 cm^2 .

Thin Film Characterization

The thickness of the films was determined using a Veeco Dektak 150 profilometer. The cross-section and surface morphology of the films were observed by scanning electron microscopy (SEM) using a Helios Nanolab 600 Dual Beam Focused Ion Beam Milling System. The porosity, pore size distribution and nanowire size were estimated from the SEM images using the Image J software. The cross-sectional TEM sample was prepared using a JEOL 9320-FIB, and the mapping of Ti and Pb was performed with a JEOL 2100 FEG TEM (EDX, X-MAX 80 mm^2). XPS with depth profiling was used to determine the atomic concentration of PbS and TiO_2 through the film depth and was converted to volumetric fractions using the molecular weight and the density of the materials. The XPS used was a PHI Versa-Probe II X-ray photoelectron spectrometer with a scanning monochromated Al source (1,486.6eV; 50 W; spot size, 200 μm), and an argon source was used for sputtering, with zalar rotation at 1 rpm.

Device Testing

A solar simulator (150 W Newport 96000 xenon arc-lamp, with AM1.5G filter and diffuser lens) was calibrated to 100 mA cm^{-2} using a silicon reference cell. J-V curves were obtained by applying an external bias to the devices and measuring the resulting photocurrent, with a Keithley 6487 picoammeter. External quantum efficiency (EQE) spectra were obtained from

300 nm to 1100 nm without bias illumination, and the useful range of data from ~ 300 nm to 900 nm was presented.

References

- (1) Kim, S. Y. Simultaneous Determination of Refractive Index, Extinction Coefficient, and Void Distribution of Titanium Dioxide Thin Film by Optical Methods. *Appl. Opt.* **1996**, *35*, 6703-6707.
- (2) Bohren, C. F.; Huffman, D. R. A Potpourri of Particles. In *Absorption and Scattering of Light by Small Particles*, Wiley-VCH Verlag GmbH: 2007; pp 181-223.
- (3) Moreels, I.; Kruschke, D.; Glas, P.; Tamm, J. W. The Dielectric Function of PbS Quantum Dots in a Glass Matrix. *Opt. Mater. Express* **2012**, *2*, 496-500.
- (4) Dang, C.; Lee, J.; Breen, C.; Steckel, J. S.; Coe-Sullivan, S.; Nurmikko, A. Red, Green and Blue Lasing Enabled by Single-Exciton Gain in Colloidal Quantum Dot Films. *Nat. Nanotechnol.* **2012**, *7*, 335-339.
- (5) Dullien, F. A. L.; Brenner, H. *Porous Media: Fluid Transport and Pore Structure*. Elsevier Science: 1991.
- (6) Johnson, P. B.; Christy, R. W. Optical Constants of the Noble Metals. *Phys. Rev. B* **1972**, *6*, 4370-4379.
- (7) Palik, E. D. *Handbook of Optical Constants of Solids*. Academic Press: 1998.
- (8) Turkevich, J.; Stevenson, P. C.; Hillier, J. A Study of the Nucleation and Growth Processes in the Synthesis of Colloidal Gold. *Disc. Faraday Soc.* **1951**, *11*, 55-75.
- (9) Zhang, Q.; Li, N.; Goebel, J.; Lu, Z.; Yin, Y. A Systematic Study of the Synthesis of Silver Nanoplates: Is Citrate a “Magic” Reagent? *J. Am. Chem. Soc.* **2011**, *133*, 18931-18939.
- (10) Hines, M. A.; Scholes, G. D. Colloidal PbS Nanocrystals with Size-Tunable Near-Infrared Emission: Observation of Post-Synthesis Self-Narrowing of the Particle Size Distribution. *Adv. Mater.* **2003**, *15*, 1844-1849.
- (11) Ip, A. H.; Thon, S. M.; Hoogland, S.; Voznyy, O.; Zhitomirsky, D.; Debnath, R.; Levina, L.; Rollny, L. R.; Carey, G. H.; Fischer, A.; et al. Hybrid Passivated Colloidal Quantum Dot Solids. *Nat. Nanotechnol.* **2012**, *7*, 577-582.
- (12) Courchesne, N.-M. D.; Klug, M. T.; Chen, P.-Y.; Kooi, S. E.; Yun, D. S.; Hong, N.; Fang, N. X.; Belcher, A. M.; Hammond, P. T. Assembly of a Bacteriophage-Based Template for the Organization of Materials into Nanoporous Networks. *Adv. Mater.* **2014**, *26*, 3398-3404.